Title

Structural transitions in the GTP cap visualized by cryo-electron microscopy of catalytically inactive microtubules

Journal

Proceedings of the National Academy of Sciences of the United States of America, 119(2)

ISSN

0027-8424

Authors

LaFrance, Benjamin J
Roostalu, Johanna
Henkin, Gil
et al.

Publication Date

2022-01-11

DOI

10.1073/pnas.2114994119

Peer reviewed

Structural transitions in the GTP cap visualized by cryo-electron microscopy of catalytically inactive microtubules

Benjamin J. LaFrance[a], Johanna Roostalu[b,1], Gil Henkin[b,c], Basil J. Greber[d,e,2], Rui Zhang[d,e,3], Davide Normanno[c], Chloe O. McCollum[a], Thomas Surrey[b,c,f,4], and Eva Nogales[a,d,e,g,4]

[a]Department of Molecular and Cell Biology, University of California, Berkeley, CA 94720; [b]The Francis Crick Institute, London NW1 1AT, United Kingdom; [c]Centre for Genomic Regulation, Barcelona Institute of Science and Technology, 08003 Barcelona, Spain; [d]California Institute for Quantitative Biosciences, University of California, Berkeley, CA 94720; [e]Molecular Biophysics and Integrative Bioimaging Division, Lawrence Berkeley National Laboratory, Berkeley, CA 94720; [f]Catalan Institution for Research and Advanced Studies (ICREA), 08010 Barcelona, Spain; and [g]HHMI, University of California, Berkeley, CA 94720

Edited by Thomas Pollard, Molecular, Cellular and Developmental Biology, Yale University, New Haven, CT; received August 13, 2021; accepted November 23, 2021

Microtubules (MTs) are polymers of αβ-tubulin heterodimers that stochastically switch between growth and shrinkage phases. This dynamic instability is critically important for MT function. It is believed that GTP hydrolysis within the MT lattice is accompanied by destabilizing conformational changes and that MT stability depends on a transiently existing GTP cap at the growing MT end. Here, we use cryo-electron microscopy and total internal reflection fluorescence microscopy of GTP hydrolysis–deficient MTs assembled from mutant recombinant human tubulin to investigate the structure of a GTP-bound MT lattice. We find that the GTP-MT lattice of two mutants in which the catalytically active glutamate in α-tubulin was substituted by inactive amino acids (E254A and E254N) is remarkably plastic. Undecorated E254A and E254N MTs with 13 protofilaments both have an expanded lattice but display opposite protofilament twists, making these lattices distinct from the compacted lattice of wild-type GDP-MTs. End-binding proteins of the EB family have the ability to compact both mutant GTP lattices and to stabilize a negative twist, suggesting that they promote this transition also in the GTP cap of wild-type MTs, thereby contributing to the maturation of the MT structure. We also find that the MT seam appears to be stabilized in mutant GTP-MTs and destabilized in GDP-MTs, supporting the proposal that the seam plays an important role in MT stability. Together, these structures of catalytically inactive MTs add mechanistic insight into the GTP state of MTs, the stability of the GTP- and GDP-bound lattice, and our overall understanding of MT dynamic instability.

microtubules | cryo-EM | GTP | TIRF microscopy | dynamic instability

Microtubules (MTs) for m by self-assembly of GTP-bound αβ-tubulin heterodimers into a cylinder consisting of laterally associated linear protofilaments (pfs) (Fig. 1*A*). During incorporation into the MT lattice, GTP hydrolysis is triggered by the catalytic glutamate in α-tubulin (E254), which becomes juxtaposed to the GTP in β-tubulin at the longitudinal interface between dimers. GTP hydrolysis has a destabilizing effect on the MT structure, and polymerization can only continue in the presence of a GTP-tubulin cap at the growing end of the MT. Stochastic loss of this cap is thought to lead to catastrophe, the switching into a depolymerization phase (1–3). The change between the stable GTP-tubulin and the metastable GDP-tubulin lattices is therefore at the heart of the phenomenon of MT dynamic instability, which is critical to MT function in the cell (4).

Given the critical nature of the GTP-to-GDP transition for MT dynamics and the nucleotide-specific recruitment of specialized factors to the MT lattice, it is critical to understand the nuanced structural differences between the nucleotide states within the MT. Previous cryo-electron microscopy (cryo-EM) studies have made use of non- or slowly-hydrolyzable GTP analogs to generate surrogates of different MT lattices (5–9). However, two GTP analogs, GMPCPP and GTPγS, give rise to different MT lattices. Whereas GMPCPP-bound MTs have an "expanded" longitudinal repeat (the dimer rise) and display a slightly positive pf twist, GTPγS-bound MTs are compacted and display a negative pf twist, both being distinct from GDP-bound MTs that are compacted and have hardly any pf twist (9). For clarification, we define "expanded" lattices as those that have a dimer rise >83 Å and "compacted" lattices as those that have a dimer rise <82 Å. Furthermore, "expanded" and "compacted" are used as terms relative to one another rather than defined against a standard MT structure. A twist = 0° would indicate that tubulin dimers are stacked in perfect vertical alignment to one another (i.e., that the pfs run parallel to the MT axis) (Fig. 1*A*). Because GMPCPP strongly promotes MT nucleation and growth, in contrast to GTPγS, GMPCPP has often been

Significance

Microtubules (MTs) are nonequilibrium polymers that switch between states of growth and shrinkage. This property is critical for their function and is a consequence of GTP hydrolysis in the MT. The structure of the stable GTP part of the MT (the GTP cap) has previously been inferred from MTs polymerized with nonhydrolyzable GTP analogs. Here, we report high-resolution structures of MTs truly containing GTP, polymerized from mutated, hydrolysis-deficient tubulins. We find that GTP-MTs have an "expanded lattice" and a "closed seam," structural characteristics possibly responsible for stabilizing the GTP cap. These results provide insight into the structural transitions at growing MT ends, furthering our understanding of the bistable nature of MTs.

Author contributions: B.J.L., T.S., and E.N. designed research; B.J.L., J.R., G.H., R.Z., D.N., and C.O.M. performed research; J.R. contributed new reagents/analytic tools; B.J.L., J.R., G.H., B.J.G., R.Z., D.N., and C.O.M. analyzed data; and B.J.L., J.R., G.H., B.J.G., T.S., and E.N. wrote the paper.

The authors declare no competing interest.

This article is a PNAS Direct Submission.

[1]Present address: BioInnovation Institute, DK2200 Copenhagen, Denmark.

[2]Present address: Division of Structural Biology, The Institute of Cancer Research, London SW7 3RP, United Kingdom.

[3]Present address: Department of Biochemistry and Molecular Biophysics, Washington University in St. Louis, School of Medicine, St. Louis, MO 63110.

[4]To whom correspondence may be addressed. Email: thomas.surrey@crg.eu or enogales@lbl.gov.

This article contains supporting information online at http://www.pnas.org/lookup/suppl/doi:10.1073/pnas.2114994119/-/DCSupplemental.

Published January 7, 2022.

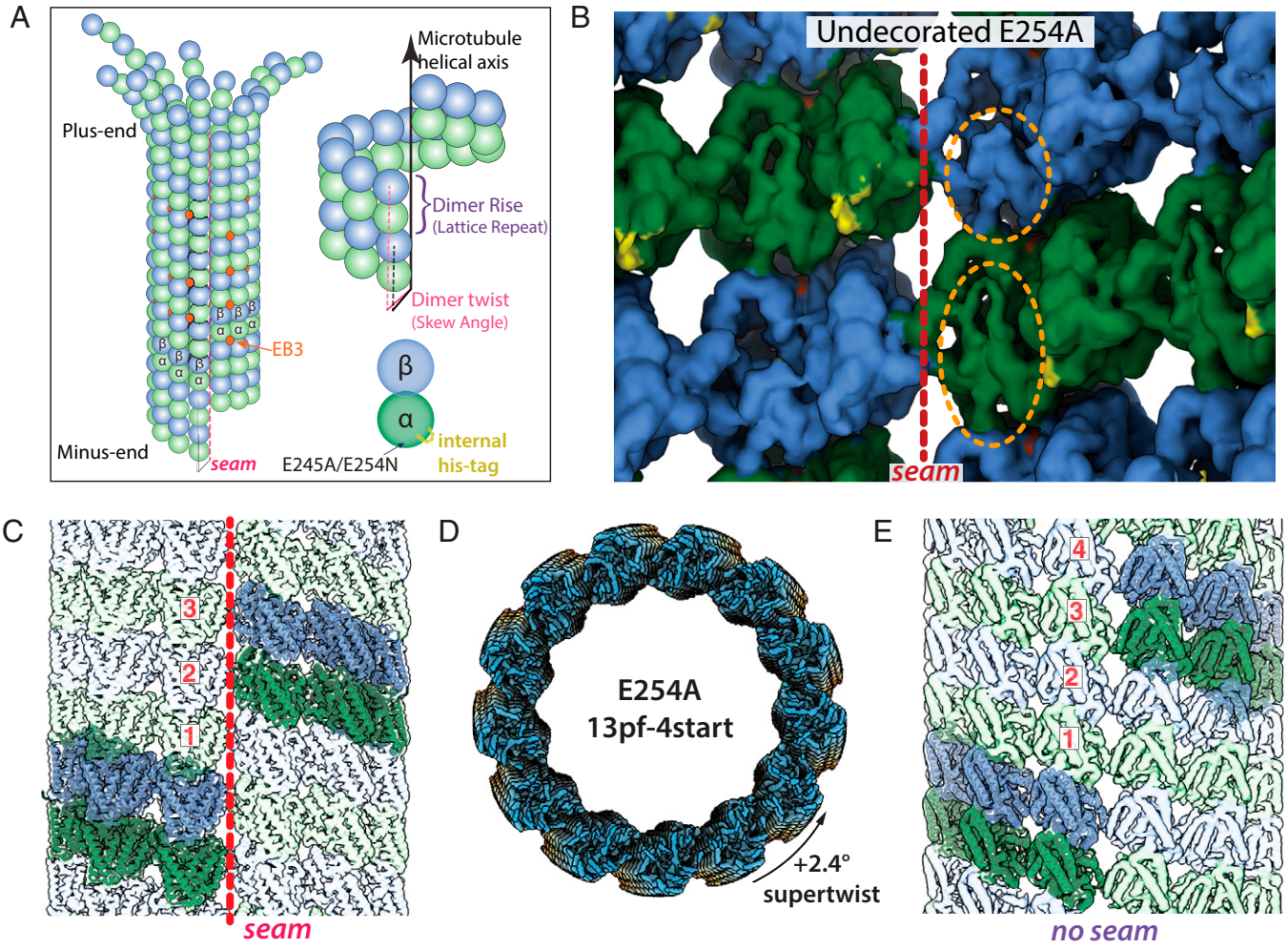

Fig. 1. Structural characterization of E254A MTs. (*A*) Cartoon diagram of a 13-pf 3-start MT undergoing depolymerization, with α-tubulin in green, β-tubulin in blue, and EB3 in orange (colors maintained throughout). Also shown are the dimer rise and dimer twist (or skew angle) of the MT lattice, in which rise denotes the distance (in angstroms) from one tubulin dimer to the one directly above it, and twist is the angle around the MT helical axis that must occur going from one dimer to the one above. (*B*) View of tubulin dimers from the lumen, in which orange ovals highlight distinctive features of the α- and β-tubulin subunits, and the red dashed line denotes the seam for E254A MTs. The small region highlighted in yellow corresponds to additional density in the recombinant sample that can be assigned to the internal His_6-tag. (*C*) A representative 13-pf 3-start MT (in this case, E254A at 3.4-Å resolution). The same generic architecture was observed for wt and E254N MTs (though with subtle differences in lattice parameters). (*D*) Subclassification of the 13-pf E254A dataset revealed a subset of 13-pf 4-start MTs, here shown colored blue-yellow-orange along the MT axis. (*E*) Lateral view of 13-pf 4-start MTs showing the absence of a seam in the MT lattice (map at 3.7 Å resolution). In *C* and *E*, one helical layer of tubulin dimers is highlighted and the corresponding ribbon diagrams docked into those dimers to emphasize the difference between the two lattices.

considered the more GTP-like analog in the context of MTs. This assumption led to the model that the MT lattice is compacted upon GTP hydrolysis due to a conformational change in α-tubulin near the longitudinal interface and the nucleotide-binding pocket in β-tubulin (5, 8–10). In this proposal, the compacted GDP state is strained and contributes to the instability of the lattice. Recent studies using X-ray fiber diffraction on an increased number of GTP analogs have suggested an alternative conformational landscape through the hydrolysis process that starts with a compacted GTP lattice that transiently expands to allow phosphate release (11). However, the structure of a GTP-bound MT lattice has not been directly visualized at high resolution. It therefore remains unclear how accurately the models derived from GTP analogs capture the structural transitions in the real GTP cap.

Another intriguing structural feature of most MTs is a seam that breaks helical symmetry. While most lateral interactions between pfs are homotypic (α-α and β-β interactions), across the seam, this interaction is heterotypic (α-β and β-α) (Fig. 1*A*) and has often been thought of as a possible point of weakness in the MT lattice (8, 9, 12–14). Indeed, comparison of stabilized MTs bound to GTP analogs with GDP-MTs have shown that while the former have a circular cross section of equally distant pfs, the less-stable GDP counterpart shows the two pfs at the seam breaking that cylindrical shape and being further apart (9). Whether this holds up for true GTP-MT segments is unknown. However, it raises the possibility that the seam may indeed be more stable in the GTP cap than in the GDP lattice and thereby contribute to the stabilizing effect of the cap.

In a complementary approach, fluorescence microscopy of end-binding proteins of the EB family binding to dynamic MTs has been used to gain indirect insight into the nucleotide and conformational state at growing MT ends (15–22). Both in cells and in reconstituted systems, EBs transiently bind with high affinity to a region at growing MT ends that comprises hundreds of tubulins and turns over within several seconds as MTs grow, generating the characteristic "end tracking" phenomenon of EBs (15, 16, 20, 23). EBs bind at the corner between four

tubulins (except along the seam), thus "reading" the dimer rise of the lattice and suggesting that their binding affinity may be sensitive to conformational changes in the MT lattice as GTP is hydrolyzed (8, 20).

We recently showed that EBs bind strongly to hydrolysis-deficient MTs polymerized from tubulin in which the catalytic glutamate in α-tubulin has been substituted by an inactive alanine (E254A) (21). Moreover, in MTs in which GTP hydrolysis is not blocked but expected to be slowed down by a glutamate to aspartate (E254D) mutation, the EB-binding region is extended, indicating that EBs indeed recognize the GTP cap (21). This also agrees with the proposal that the EB-binding region at growing MT ends protects the MT from catastrophe (18, 20). However, EBs bind only very weakly to the expanded lattice of GMPCPP-MTs, the presumed mimic of GTP-MTs, whereas they bind well to the compacted lattice of GTPγS MTs proposed to resemble a posthydrolysis state (8, 9, 20, 22). These discrepancies raised the question of whether the GTP cap really displays an expanded lattice and if yes, what the key structural features that ensure high-affinity binding of EBs to the GTP cap but not to GMPCPP-MTs or GDP-MTs are.

Here, in order to better understand the GTP conformation of MTs, we used cryo-EM to visualize MTs assembled from recombinant wild-type (wt) and mutant human tubulin in which the catalytic glutamate in α-tubulin was mutated to alanine or asparagine (E254A or E254N, respectively), making them deficient in GTP hydrolysis. We find that both of the catalytically inactive MTs are stable and have an expanded dimer rise but that they differ in their pf twist. E254A MTs display a negative twist and high EB-binding affinity. E254N MTs have a positive twist and show low EB-binding affinity, making them similar to GMPCPP-MTs. However, in contrast to GMPCPP-MTs, growing E254N MTs can switch spontaneously into a high EB-binding conformation, a transition that is promoted by EBs. These results demonstrate that GTP-MTs can adopt at least two structurally distinct expanded states. EBs promote compaction and a negative pf twist in both mutant MTs, despite the absence of GTP hydrolysis, and the MT lattice they promote probably reflects conformational features adopted by the true GTP cap in EB decorated wt MTs. Lastly, catalytically inactive mutant MTs trapped in a GTP-bound state display a regularized seam, lending further support to the hypothesis that a more "closed" seam is a critical stabilizing feature of the GTP cap. Our structures provide insights into the intrinsic regulation of MT instability and further our understanding of the prehydrolysis state of MTs and the preference of EBs for certain MT states.

Results

To better understand how nucleotide state affects MT structure, we structurally characterized MTs assembled from catalytically inactive tubulin that are constitutively locked in the GTP state. Recombinant human tubulin was purified and biochemically characterized as described previously (21) (*SI Appendix*, Fig. S1). We optimized our cryo-EM image analysis pipeline to deal with some unexpected challenges (*SI Appendix*, Fig. S2; see *Results*). All of the MT structures were determined to 3.5- to 5-Å resolution, which allowed us to make confident inferences about the dimer rise and twist parameters as well as seam location. However, given our resolution regime, we do not compare any structural differences beyond those observed for the C_α backbone and only define nucleotide state when confident. Furthermore, we focus on the results obtained for 13-pf MTs given their abundance and physiological relevance in mammalian cells (24–26), but the characteristics we describe herein also held true for 14pf MTs.

Wt Recombinant Tubulin Does Not Alter the MT Architecture. We first determined the cryo-EM structure of MTs polymerized from recombinant wt human tubulin to 3.8-Å resolution (*SI Appendix*, Fig. S2*A*). We also determined the structure of the kinesin decorated wt MT to 3.6-Å resolution, with both datasets consisting of ∼20,000 particles. Lattice parameters of these MTs, both undecorated and decorated with kinesin-1 motor domains, were nearly indistinguishable from previously reported GDP-MT structures assembled from mammalian brain tubulin (5, 8, 9) (Table 1). The dimer rise was 81.69 Å and 81.50 Å and the twist was +0.09° and +0.05, respectively, for recombinant wt human GDP-MTs and GDP-MTs from mammalian brain tubulin. However, there was additional density in the recombinant MT structure corresponding to the internal His_6-tag located within the partly disordered acetylation loop of α-tubulin that includes lysine 40 (*SI Appendix*, Fig. S2*D* and Fig. 1*B*). This purification tag has previously been shown to have no effect on polymerization dynamics (21, 27), and our current study confirms that it also does not alter lattice parameters compared to the endogenous wt mammalian MTs studied previously (Table 1) (27).

E254A MTs Have an Expanded Lattice with a Negative Twist. For the catalytically inactive mutant E254A (in α-tubulin), cryo-EM processing protocols developed for and applied to MTs (28, 29) failed to yield a high-resolution structure. Some of these E254A MTs had an abnormally large twist parameter, a feature that was also visible in raw images and 2D (two-dimensional) class averages (*SI Appendix*, Fig. S2*B*), that challenged our image analysis pipeline. Further rounds of 3D (tri-dimensional) classification after the initial classification by pf number (*SI Appendix*, Fig. S2*C*) showed that there are at least two distinct lattice conformations for 13-pf E254A MTs: one corresponding to the commonly observed 13-pf 3-start lattice (Fig. 1 *B* and *C*) and a second one with a 13-pf 4-start lattice (Fig. 1 *D* and *E*) (3.4 Å from 68,000 particles and 3.7 Å from 26,022 particles respectively). The dimer rise of the 13-pf 3-start structure was similar to the previously described GMPCPP-bound mammalian brain MTs, with a value of 83.18 Å that corresponds to an expanded lattice. However, the pf twist was negative (−0.22°) instead of positive (+0.23°) as observed for GMPCPP-MTs (Table 1). Historically, 4-start lattices have been almost exclusively observed for 15-pf and 16-pf MTs, and more rarely for 14-pf (30). Like the 13-pf 3-start MT, the 13-pf 4-start lattice of the E254A MTs was also in the expanded conformation, with a dimer rise of 83.03 Å (Table 1). Furthermore, the 4-start lattice maintains the same interpf contacts as the 3-start lattice, with the exception that all 4-start contacts were homotypic (truly helical and without a seam), while the 13-pf 3-start MTs displayed the canonical heterotypic seam (Fig. 1 *C* and *E*). In conclusion, independent of the start number of the lattice, our analysis shows E254A MTs are expanded, in contrast to the compacted lattice of GDP-MTs.

E254N MTs Switch between Different Lattice States as Indicated by EB3 Binding. To test whether the presence of GTP rather than the E254A mutation itself has an effect on the structure of the MT lattice, we generated a more-conservative E254N mutation at the catalytic site. E254N MTs grown in the presence of GTP also did not hydrolyze GTP, as demonstrated by HPLC (high-performance liquid chromatography) analysis of their nucleotide content (*SI Appendix*, Fig. S1). Next, we imaged mGFP-EB3 binding to unlabeled E254N MTs that grew from immobilized MT seeds by total internal reflection fluorescence (TIRF) microscopy (Fig. 2*A*). As expected for GTP hydrolysis–deficient MTs, they grew persistently without displaying catastrophes (kymographs in Fig. 2 *B–D*). They grew more slowly (Fig. 2 *E*, *Top*) than wt recombinant human MTs (21, 27, 31) (∼10 nm/s compared to 15 to 30 nm/s,

Table 1. Lattice parameters for select 13-pf MT structures

Sample	Lattice spacing/dimer rise (Å)	Skew/twist (°)	Intradimer rise (Å)	Interdimer rise (Å)	Reference
GMPCPP-TPX2	84.33	+0.40	41.67	42.61	(9)
GMPCPP	83.95	+0.23	41.53	42.43	(9)
GMPCPP-DCX	83.74	+0.16	NA	NA	(10)
GMPCPP-Kinesin	83.16	+0.19	41.45	42.00	(9)
GTP-E254N	83.45	+0.13	41.53	41.93	This study
GTP-E254A 3-start	83.18	−0.22	41.15	42.36	This study
GTP-E254A 4-start	83.03	+2.40	NA	NA	This study
GDP-P_i-DCX	81.74	0.00	NA	NA	(10)
GTPγS-Kinesin-EB3	81.96	−0.28	41.31	40.51	(9)
GTPγS	81.93	−0.12	41.35	40.45	(9)
GTPγS-EB3	81.52	−0.25	41.30	40.30	(8)
GTPγS-DCX	82.10	−0.02	NA	NA	(10)
GDP-DCX	81.90	+0.08	NA	NA	(10)
GDP	81.76	+0.08	41.44	40.30	(9)
EB3-GMPCPP	81.71	−0.10	41.50	40.30	(8)
wt E254-GDP-Kinesin	81.69	−0.09	41.38	40.37	This study
GTP-EB3+E254A	81.64	−0.19	41.25	40.44	This study
GDP-Kinesin	81.64	+0.01	41.38	40.36	(9)
GDP-Kinesin-EB3	81.59	−0.11	41.35	40.32	(9)
wt E254-GDP	81.50	+0.05	41.25	40.30	This study
GDP-EB3	81.44	−0.12	41.40	40.30	(8)
GTP-E254N+EB3	81.15	−0.29	41.35	40.45	This study

MT lattice parameters obtained in this study are reported alongside previously published values for reference. Expanded lattices are in blue (GMPCPP and undecorated catalytically inactive mutants), presumed transition state MTs (GDP+P_i or GTPγS) are colored in green, and compacted lattices are shaded in red (GDP state or catalytically inactive mutants + EB3). NA signifies cases in which intradimer or interdimer values were not reported due to mixing of α/β-tubulin subunits or in which resolution was too low to accurately determine the values.

respectively). Remarkably, the MTs display segments with different properties, as reflected by the long stretches of either weak or strong mGFP-EB3 signals, indicating that the GTP lattice can be in at least two different conformations that are both stable (Fig. 2*A* and Movies S1 and S2). Occasionally the MT conformation switched suddenly at the growing MT end from a weak to high EB3 binding-affinity state that then persisted as the MT grew (Fig. 2*B* and Movie S3; all three MTs shortly after having started to grow). The opposite switch from growing a strongly EB3-binding lattice to a weakly EB3-binding lattice at the growing MT end was not observed, suggesting that the high-affinity conformation is preferred but that this conformational state is hard to access when the MT has started growing with a low-affinity lattice. The position of the resulting boundary between lattices in the two conformations was either immobile (Fig. 2*C* and Movie S3, *Middle*) or could slowly move, either to the MT plus end (Fig. 2*B* and Movie S3, *Top*) or the minus end (Fig. 2*D* and Movie S3, *Bottom*), indicative of a slow and remarkably cooperative lattice transformation at the boundary either from high-to-low or from low-to-high EB3-binding affinity, respectively.

Increasing the EB3 concentration affected the relative stability of the two conformational lattice states. While an overall average increase of the mGFP-EB3 fluorescence along the E254N MTs was observed as the EB3 concentration was increased from 5 to 40 nM (Fig. 2 *E*, *Bottom*), segments with higher and lower EB3-binding density were still present at all concentrations studied. At higher EB3 concentrations, more strongly EB3-binding segments and fewer weakly EB3-binding segments were observed (Fig. 2*F*). Moreover, with increasing EB3 concentration, slow lattice transformations at the boundary between two segments from weak to high EB3-binding affinity became more frequent. This demonstrates that EB3 promotes the formation of its high-affinity binding conformation of E254N MTs.

mGFP-EB3 fluorescence line profiles and intensity histograms demonstrated that the segmented strong and weak mGFP-EB3 binding to E254N MTs was clearly different from the previously described, more-uniform high-affinity mGFP-EB3 binding to E254A MTs (21) (Fig. 3 *A* and *B*). Particularly, the intensity histograms show the appearance of a second, high-affinity EB3-binding state for E254N MTs with increasing EB3 concentration (Fig. 3 *B*, *Right*), explaining why EB3 binding increases more than linearly with increasing EB3 concentration in the tested concentration range in contrast to the less-variable EB3 binding to E254A MTs (Fig. 3*C*). Plotting the SD of mGFP-EB3 intensity against the mGFP-EB3 intensity also confirms that E254A MTs display a less heterogenous lattice state with respect to EB3-binding than E254N MTs, although some EB3-binding variation is also observable for E254A MTs (Fig. 3*D*).

These TIRF microscopy experiments show that the two GTP hydrolysis–deficient mutant MTs studied here both can adopt a high-affinity binding conformation for EBs. However, E254N MT additionally display a low-affinity conformation that can switch into the high-affinity conformation during growth, a switch that is promoted by EB-binding.

E254N MTs Have an Expanded Lattice with a Positive pf Twist in the Absence of EB3. Next, we used cryo-EM to determine the lattice parameters of E254N MTs (3.8-Å resolution from 13,706 particles). In contrast to E254A MTs, we did not detect a prominent population of 13-pf 4-start MT species in the E254N MTs despite our numerous classification attempts (although we cannot completely exclude the possibility of a very rare 4-start lattice subpopulation). The 13-pf 3-start E254N MTs showed an expanded dimer rise of 83.45 Å, similar to E254A MTs. However, in contrast to E254A MTs, the pf twist was positive with an angle of +0.13° (Table 1). The lattice parameters of E254N MTs are similar to GMPCPP-MTs, in which the lattice has a rise of 83.95 Å and a twist of +0.23°. Furthermore, both E254N and E254A structures showed homotypic lateral interactions that appear identical, at the resolution of our study, to those seen in the wt lattice as well as GMPCPP-MTs. Comparison of backbone deviations for the tubulin dimer between the E254N

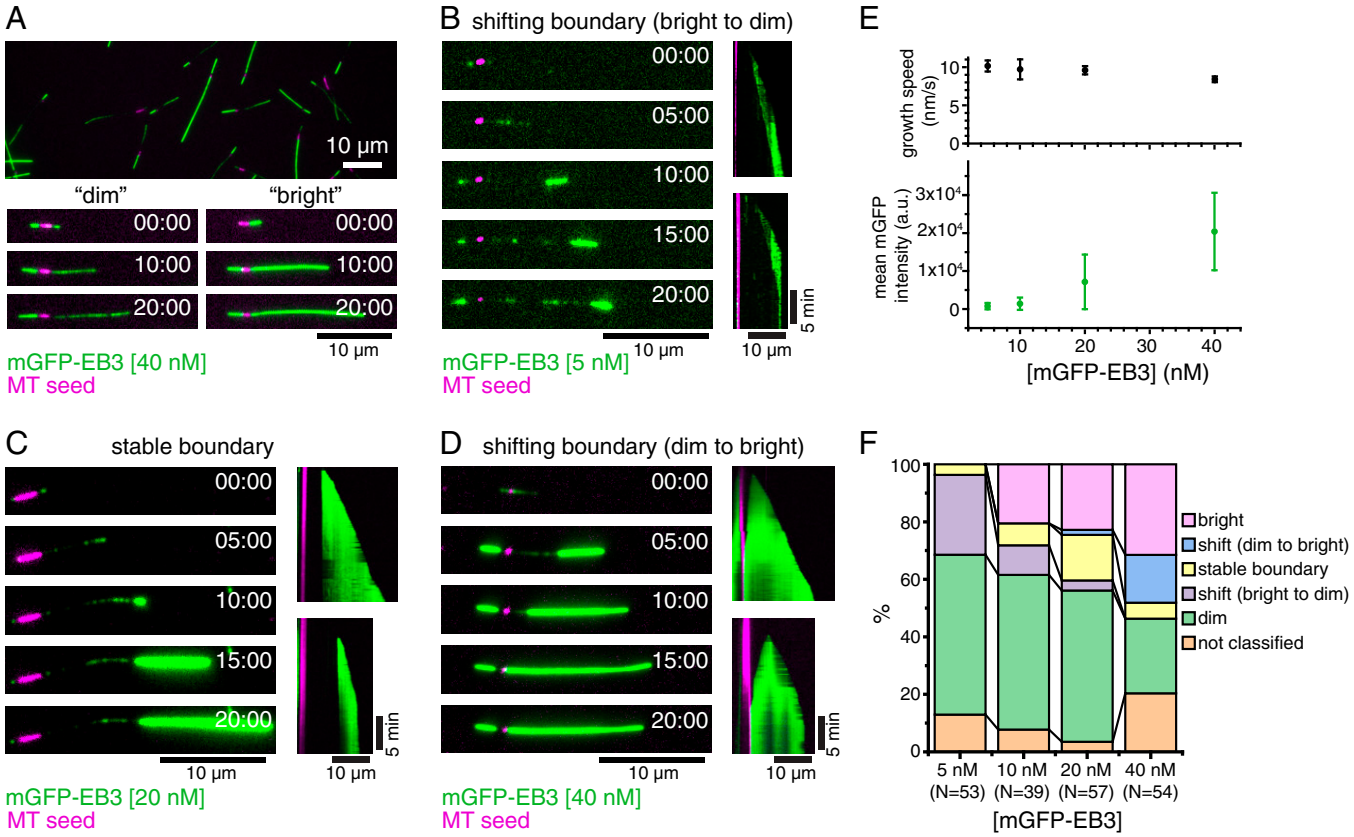

Fig. 2. Dynamic E254N MTs observed by TIRF microscopy. (*A*) TIRF microscopy image of nonfluorescent E254N MTs after 20 min of growth from CF640R-labeled, GMPCPP-stabilized MT "seeds" (magenta) in the presence of 40 nM mGFP-EB3 (green) and GTP showing a variety of "dimly" and "brightly" mGFP-EB3-decorated MTs. (*Bottom*) Time series of growth of a "dim" and "bright" MT. (*B–D*) Time series and kymographs exemplifying MT growth behavior: (*B*) MT showing a switch from "dim" to "bright" lattice at the growing plus end, followed by progressive conversion of the lattice at the boundary to the "dim" state, causing the boundary to move toward the growing plus end (5 nM mGFP-EB3). (*C*) Once this MT switches into a "bright" binding state at the growing plus end, the boundary between the "dim" and the "bright" lattice does not change (20 nM mGFP-EB3). (*D*) Once this MT switches to the "bright" state, the "dim" lattice progressively switches at the boundary toward the seed, until the MT is entirely "bright" (40 nM mGFP-EB3). (*E*, *Top*) Mean E254N MT plus-end growth speed for the different mGFP-EB3 concentrations studied. Error bars represent SEs. The numbers of MTs and segments of constant speed used in the calculation for each mGFP-EB3 concentration are the following: 5 nM mGFP-EB3, 42 MTs, and 109 segments; 10 nM mGFP-EB3, 30 MTs, and 74 segments; 20 nM mGFP-EB3, 50 MTs, and 169 segments; and 40 nM mGFP-EB3, 42 MTs, and 124 segments). (*Bottom*) Mean fluorescence intensity of mGFP-EB3 binding to MTs for each mGFP-EB3 concentration. Error bars represent SDs. Intensity data are replotted in Fig. 3C. (*F*) Stacked bar chart of MT growth behavior at different mGFP-EB3 concentrations. mGFP-EB3 binding patterns were assessed manually by comparing to the other MTs in the same field of view. "Dim" and "bright" MTs showed relatively uniform binding throughout growth. Some MTs could not be clearly classified into any category. Only the parts of the MTs growing from the plus end of stabilized MT seeds were included in the analysis reported. N indicates the number of MTs considered for analysis from two different experimental replica (three for 20 nM mGFP-EB3). All experiments were performed with 12.5 µM E254N tubulin. (Scale bars, 10 µm for length and 5 min for time.)

MTs and either GMPCPP-MTs or GDP-MTs clearly shows the E254N and GMPCPP similarity (*SI Appendix*, Fig. S3). This indicates that GTP-MTs in the absence of EBs tend to have an expanded MT lattice, but mutant hydrolysis-deficient GTP-MTs can display different pf twists depending on the particular mutant, revealing an unexpected plasticity of the GTP lattice.

Because the weakly EB3-binding E254N lattice conformation dominated at low EB3 concentrations in our TIRF microscopy experiments, we assign the cryo-EM structure obtained in the absence of EB3 to the weakly EB3-binding lattice conformation observed in TIRF microscopy. This is also in agreement with GMPCPP-MTs, which bind EB3 only very weakly and display similar lattice parameters as E254N MTs in the absence of EB3 (9).

EB3 Compacts Both E254N and E254A MTs. Previous cryo-EM work has shown that EB3 has the ability to promote MT compaction and even induce GMPCPP hydrolysis in GMPCPP-MTs (8). Here, we observed by TIRF microscopy that EB3 can induce a conformational change in GTP containing E254N MTs revealed by a change in EB-binding affinity (Figs. 2 and 3). We therefore sought to see what effect EB3 could have at a structural level on the mutant MTs that were locked in a GTP-bound state. Addition of saturating concentrations of the MT-binding domain of EB3 to preformed E254N MTs caused the MT dimer rise to decrease from 83.45 Å to 81.15 Å, indicative of a lattice compaction toward the GDP-like conformation (Table 1 and Fig. 4 *A* and *B*). A compacted lattice has also been observed for the γ-phosphate containing GTPγS-EB3 MT lattice (8). The pf twist of −0.29° shown for E254N-EB3 MTs agrees well with previous structures of MTs decorated with EB3 that also showed a pf twist of around −0.3° (8, 9). Therefore, we assigned this cryo-EM structure to the strongly EB3-binding lattice conformation of E254N MTs observed by TIRF microscopy. Given the diversity of EB3-binding lattices shown for E254N MTs in our TIRF experiments, we employed the layer line analysis technique utilized by Zhang et al. to separate strongly and weakly EB3-binding regions of MTs (9). However, we were unable to classify any distinct lattices besides the strongly EB3-binding structure reported here. Furthermore, due to a limited resolution of 5 Å

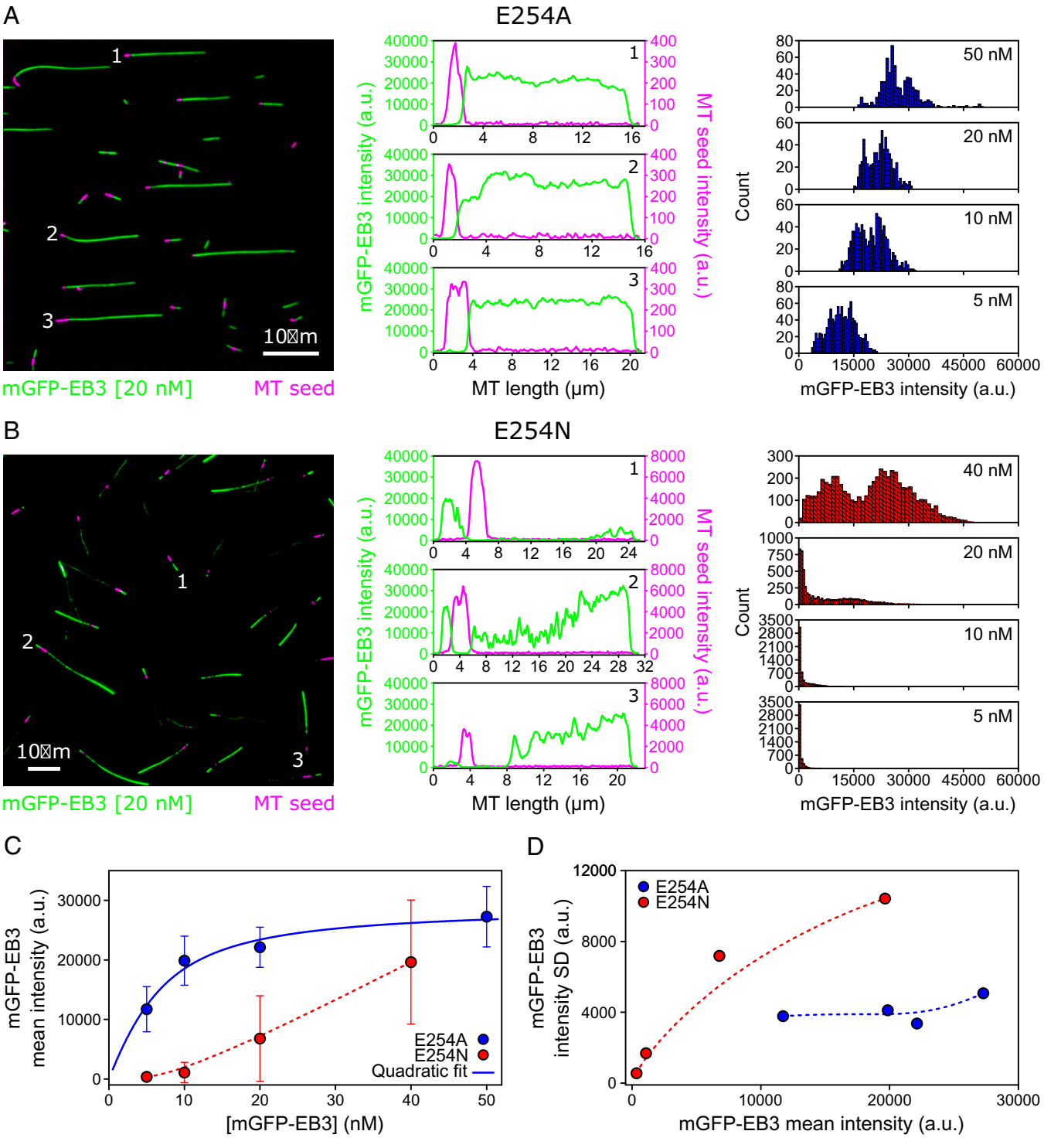

Fig. 3. Quantitative comparison of mGFP-EB3 binding to E254A and E254N MTs as observed by TIRF microscopy. (*A* and *B*, *Left*) TIRF microscopy images of nonfluorescent E254A MTs (*A*) and E254N MTs (*B*) grown from CF640R-labeled, GMPCPP-stabilized "seeds" (magenta) in the presence of 20 nM mGFP-EB3 (green) and GTP. (Scale bars, 10 μm.) (*Middle*) Line profiles of mGFP-EB3 (green) and MT seed (magenta) intensities along the three MTs indicated in the images on the *Left*. (*Right*) Global mGFP-EB3 intensity distribution along several MTs at different mGFP-EB3 concentrations (E254A MTs: 5 nM mGFP-EB3, n = 18 MTs; 10 nM mGFP-EB3, n = 13 MTs; 20 nM mGFP-EB3, n = 10 MTs; and 50 nM mGFP-EB3, n = 11 MTs; E254N MTs: 5 nM mGFP-EB3, n = 35 MTs; 10 nM mGFP-EB3, n = 37 MTs; 20 nM mGFP-EB3, n = 43 MTs; and 40 nM mGFP-EB3, n = 38 MTs). (*C*) Mean intensity of mGFP-EB3 along E254A MTs (blue circles) and E254N MTs (red circles; same data as in Fig. 2 *E*, Bottom) as a function of mGFP-EB3 concentration. Error bars represent SDs. The solid blue line shows a quadratic fit through the E254A MT data, and the red dashed line is a Bezier interpolation used as guide-to-the-eye. (*D*) SD of mGFP-EB3 intensity along the MTs as a function of mGFP-EB3 mean intensity for E254A MTs (blue circles) and E254N MTs (red circles). Dashed lines are Bezier interpolations used as guide-to-the-eye.

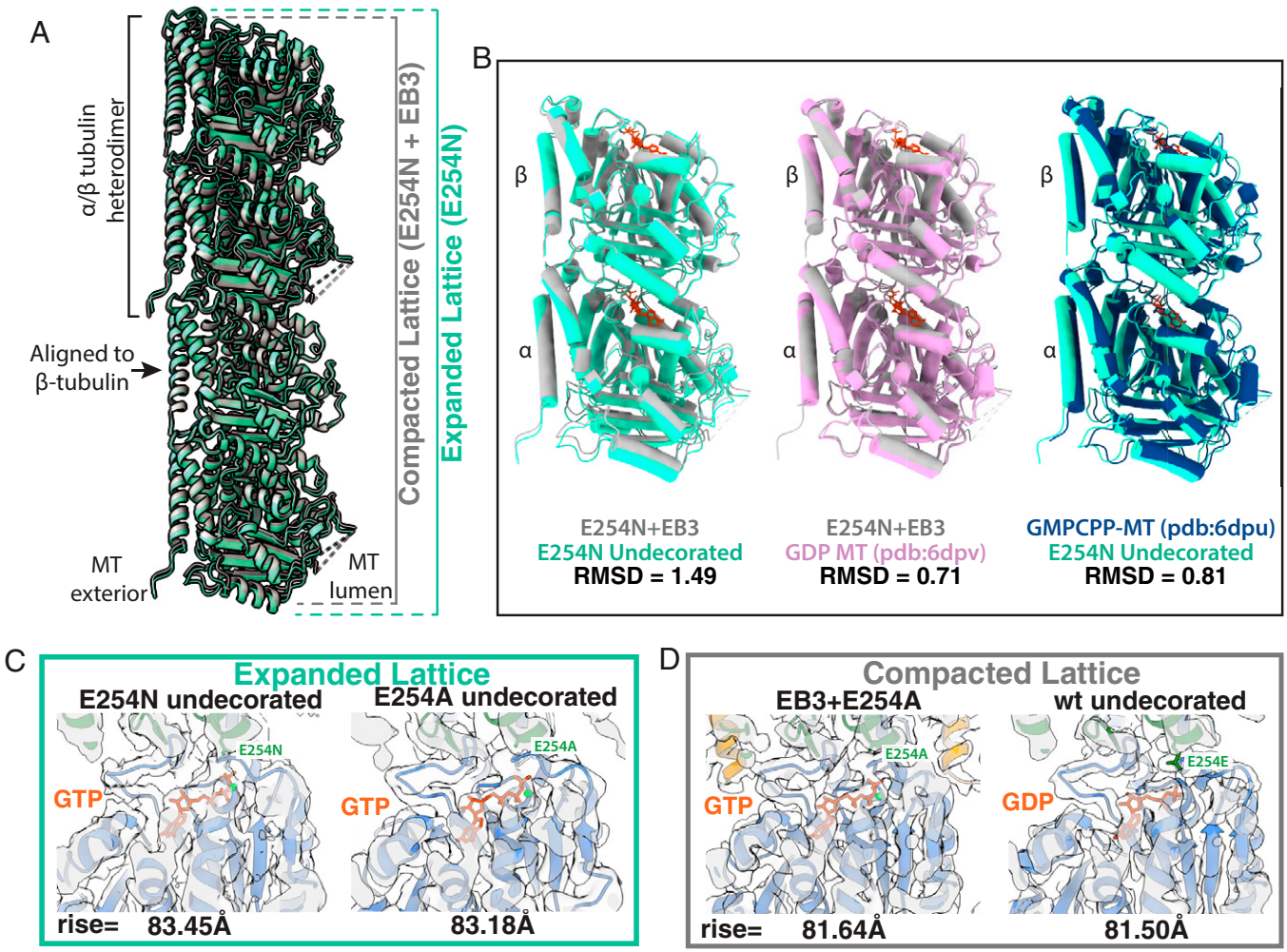

Fig. 4. GTP state and compaction for wt, E254N, and E254A MTs. (*A*) Visualization of how the MT axial repeat changes, either through hydrolysis of GTP or through EB3 binding to catalytically inactive MTs. Specifically, the panel shows atomic models for the structures determined herein, with the undecorated E254N MT shown in green and E254N+EB3 MT in gray. (*B*) Comparison of tubulin heterodimers to show the structural changes that occur upon compaction. Dimers are aligned onto β-tubulin, which has been shown to undergo the least amount of conformational changes in previous studies and herein. RMSD values are reported below each comparison. (*C*) Expanded lattices, with a rise >83 Å and with clear GTP density. Shown here as examples of expanded lattices for undecorated E254N (3.8 Å) and undecorated E254A (3.4 Å) maps. (*D*) Compacted lattices with a rise <82 Å can be formed by EB3 binding (while maintaining GTP) or by hydrolysis into the GDP state. Examples for the compacted lattices observed are EB3+E254A (3.5 Å) and the undecorated wt lattice (3.8 Å).

for the EB3-decorated E254N MTs, we could not definitively resolve the nucleotide state.

This same compaction phenomenon was observed for the E254A MTs polymerized in the presence of EB3. The EB3 occupancy was higher in this case, likely due to the higher affinity of EB3 binding to the E254A lattice (Fig. 3*C*). The dimer twist was found to be −0.19° for the 13-pf 3-start E254A MTs grown in the presence of EB3 (Table 1). The structure of the EB3-bound E254A MT (3.5-Å map from 56,705 MT segments or "particles") clearly shows that the GTP present in the undecorated mutant MTs (Fig. 4*C*) is still present in the active site (Fig. 4*D*) despite the MTs sampling a compacted state. These data suggest that lattice compaction can occur without hydrolysis, regardless of whether EB3 is added before or after MT formation. Overall, these data continue the trend that EB3 compacts MTs and promotes a more-negative MT twist.

The MT Seam Opens upon GTP Hydrolysis. It is generally accepted that during MT growth, individual tubulin dimers experience a certain amount of strain to accommodate the lattice architecture (1). This strain is thought to increase after GTP hydrolysis, thus eventually promoting depolymerization (1, 8, 9). During MT-shortening, lateral contacts are lost first, pfs curl outwards, and eventually longitudinal contacts break down. Due to the heterotypic αβ-tubulin interactions formed across the seam, the seam has been considered a potential weak point of the MT lattice in which "peeling" of pfs could start (8, 9). By calculating displacement values between a symmetrized and an asymmetric (C1) reconstruction (8, 9), we previously found that in mammalian brain GDP-MTs, the pfs at the seam break cylindrical symmetry and appear separated with respect to the rest (we see the same for recombinant, wt MTs; Fig. 5*A*), while this characteristic is either missing or less pronounced in the case of MTs containing nonhydrolyzable GTP analogs (8, 9). The presence of EB3, which binds between pfs, regularizes the seam, irrespective of nucleotide content (Fig. 5*B*). Here, we found that E254N and E254A MTs also do not show any pf opening at the seam either in the absence (Fig. 5 *C* and *D*) or presence of EB3 (Fig. 5*E*) (refer also to Movie S4 for a morph between E254N MTs and wt MTs showing the rotation of pfs proximal to the seam). These results add further experimental support for the proposal of lateral tubulin interactions at the seam being

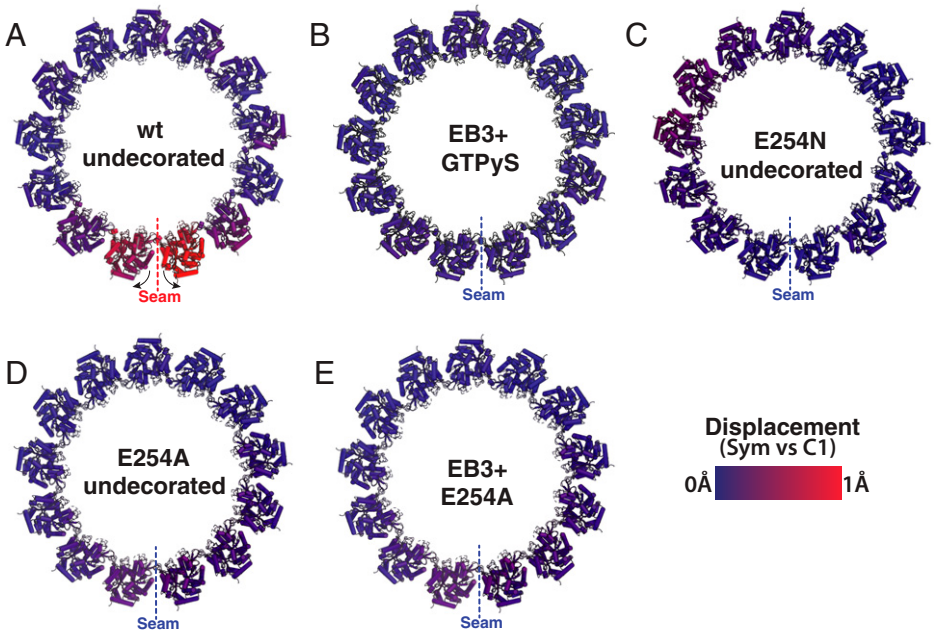

Fig. 5. Seam opening correlates with GTP hydrolysis and MT instability. The panels correspond to MT cross-sections for both GTP-like and GDP-MTs showing comparison between the symmetrized and C1 maps to illustrate the break of symmetry with the opening between pfs at the seam for some of the MTs studied. (*A*) Wt MTs in a posthydrolysis state show the seam-opening phenomenon localized to the pfs at the seam. Movie S4 allows for a dynamic visualization of this motion. (*B*) GTPγS copolymerized with EB3 originally from data collected for the map deposited as EMD-6347 (8). (*C*) Undecorated E254N MTs. (*D*) Undecorated E254A MTs. (*E*) The E254A MT copolymerized with EB3. No seam opening is seen for *B*, *C*, *D*, or *E*.

stronger before GTP hydrolysis, and the seam possibly becoming the weak lateral interface within the MT lattice after GTP hydrolysis (8, 9).

Discussion

Here, we have determined high-resolution cryo-EM structures of MTs with GTP bound at the exchangeable nucleotide-binding site by visualizing GTP hydrolysis–deficient MTs generated by polymerizing recombinant human tubulin with either a E254A or E254N substitution in α-tubulin. This approach is complementary to previous studies of wt MTs grown in the presence of different GTP analogs. Both amino acid substitutions in recombinant tubulin produced MTs lacking catastrophes, as expected for GTP-MTs. Structural analysis revealed that both E254A and E254N MTs display an expanded MT lattice, as was previously described for GMPCPP-MTs (5, 32) but not for GTPγS or BeF_3^- MTs (8, 11). On the other hand, the lattices of the two types of mutant GTP-MTs were not identical, exhibiting different pf twist parameters.

When growing as a 13-pf 3-start lattice, which is the lattice that is typically observed in human cells, E254A MTs displayed a negative pf twist, in contrast to the positive twist observed for 13-pf 3-start E254N MTs and previously studied GMPCPP-MTs. Our observations with hydrolysis-deficient MTs and previous studies with MTs grown with slowly hydrolysable GTP analogs demonstrate a remarkable plasticity of the GTP(-like) MT lattice (1, 8, 11). Furthermore, small changes at the longitudinal tubulin–tubulin interface, either in the nucleotide itself or in the normally catalytic residue, can have a profound impact on MT structure. The fact that the tubulin residues critical for hydrolysis also provide interactions at the polymerization interface makes mutated, catalytically inactive MTs sensitive to specific changes of this residue.

Regarding the 13-pf 4-start lattice observed for the E254A mutant, different start numbers for MTs have been characterized previously, though rarely were they in 13-pf lattices (30). Perhaps the conditions used in our cryo-EM studies allowed the E254A MTs to display a variety of lattice structures with respect to pfs and start number—possibly a consequence of high stability of these MTs (21). Of note, the 13-pf 4-start phenomenon has also been observed recently in a GDP-BeF_3^- analog (11), but it was not analyzed further. The unexpected lattice plasticity of these MTs may indicate increased flexibility of the GTP-bound state that could play a functional role during tubulin incorporation into the MT and its recognition by cellular factors. However, the E254A 13-pf 4-start structure could also be due to the mutation itself.

Another interesting question is what is the lattice structure recognized by EBs? MTs with high EB-binding affinity all have a negative pf twist, even in the absence of EBs (GTP-E254A, GTPγS-wt, and BeF_3^--wt) (9, 11, 22). MTs to which EBs only bind weakly show either minimal pf twist of ∼0.1 Å (GDP-wt) or they show a positive twist (GMPCPP-wt and GTP-E254N) (8, 9). Moreover, when EB3 is forced to bind to lattices with a positive pf twist (GMPCPP-wt and GTP-E254N) under saturating conditions, the pf twist becomes negative, suggesting that the high-affinity conformation of the EB-binding site at the corners of four tubulins requires a negative pf twist (8). Additionally, EB3 binding at saturating conditions compacts normally extended MT lattices (GMPCPP-wt, GTP-E254N, and GTP-E254A), irrespective of whether the nucleotide can be hydrolyzed (GMPCPP-wt) or not (GTP-E254N and GTP-E254A) (9). The compaction of the GTP lattice may be somewhat inhibited in E254N MTs, explaining their segmented appearance, while it occurs more easily in E254A MTs, explaining the higher affinity of EB binding to E254A MTs. Given that EBs have the ability to compact GTP-bound MTs and to accelerate a conformational transition toward the GDP lattice (33), it is likely that EB3-driven compaction precedes hydrolysis in wt MTs growing in the presence of GTP, a model recently proposed based on studies of multiple GTP analogs (1, 11).

Taken all this information together, we favor a model for the structure of the GTP cap in wt MTs in which the GTP lattice transitions through several conformations before forming a

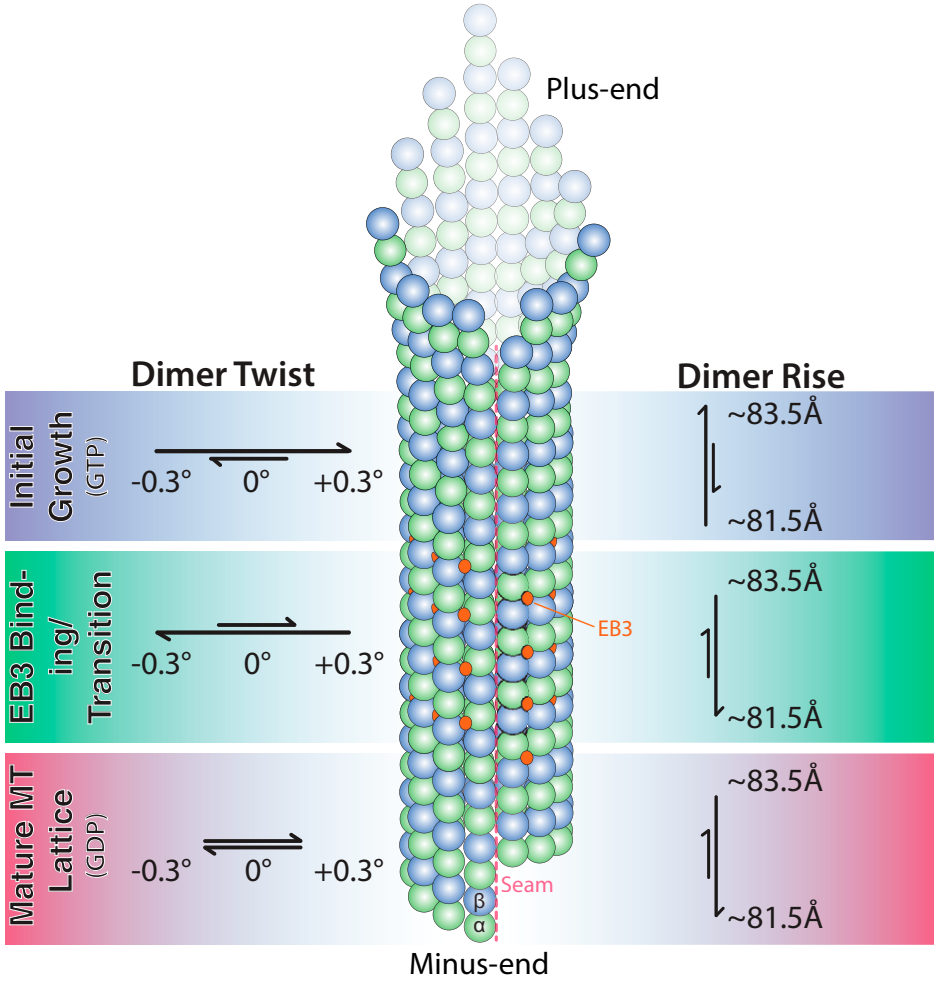

Fig. 6. Model of MT growth informed by cryo-EM and TIRF microscopy observations.

mature GDP lattice (Fig. 6). Initially, freshly formed pfs would be in an expanded state, possibly sampling conformations corresponding to what is observed in GTP-E254A, GTP-E254N, and GMPCPP-MTs. Such lattices are likely to be only short lived, otherwise there would be a longer EB-undecorated part before the "EB comet" starts at the growing end of wt MTs. The high-affinity EB-binding region likely has a negative twist, possibly transitioning from an expanded GTP-E254A–like lattice to a compacted GTPγS-wt–like lattice, in agreement with recent evidence suggesting that the GTPγS lattice also corresponds to a GTP state (11). How fast this transition takes place remains unknown, because both lattices show high EB-binding affinity. Hydrolysis followed by phosphate release would then cause the pf twist to become ∼0° in the GDP lattice to which EBs only bind weakly.

The exact interactions within the MT lattice that confer greater stability in the GTP lattice relative to the GDP lattice remain unclear, at least in part because no high-resolution structure of a true GTP-wt lattice is available. We have previously proposed that the tension present in the GDP lattice may manifest as a seam-opening phenomenon. Our present study, using hydrolysis mutants instead of GTP analogs, further supports such a model, as the stable hydrolysis-inactive MTs all exhibit a "closed" seam structure, as do GMPCPP and GTPγS MTs as well as MTs stabilized by drugs (8, 9, 34). Thus, MT seam stability may serve as a proxy for overall MT stability. The more-symmetric pf arrangement around the MT axis observed for the E254N and E254A mutant (Fig. 5 *C* and *D*),and for GMPCPP-MTs (8, 9) is associated with the more-stable GTP region of MTs. On the other hand, the outward rotation of the seam-proximal pfs in GDP-MTs, both for the wt MTs described here (Fig. 5*A*) and the previously described porcine MTs (9), may reflect tension buildup at the seam resulting from GTP hydrolysis.

Conclusions

Recent advances in the production of recombinant tubulin have opened the door to new structure–function studies of MTs. In this work, we utilized recombinant human tubulin to better understand the effect of GTP hydrolysis on MT structure and stability and thus the mechanistic basis of the property of dynamic instability essential for MT cellular function. We show that hydrolysis-impaired E254A and E254N mutant MTs display an expanded lattice conformation and a seam lacking the structural sign of strain seen in GDP-MTs that have undergone nucleotide hydrolysis (8, 9). Our mutant studies provide additional insights into the conformational dynamics that accompany the GTP-to-GDP transition in MTs, suggesting a series of transitions from an expanded to a compacted lattice with accompanying changes also in pf twist. Future studies visualizing the ends of dynamic MTs with high resolution will ultimately allow us to observe the true GTP cap and test the model for its structure proposed here.

Table 2. Buffers for the purification of recombinant tubulin

Buffer	Composition
Lysis	80 mM PIPES, 1 mM EGTA, 6 mM $MgCl_2$, 50 mM imidazole, 100 mM KCl, 2 mM GTP, 1 mM BME, and pH 7.2 + protease inhibitors and DNase
Dilution	80 mM PIPES, 1 mM EGTA, 6 mM $MgCl_2$, 50 mM imidazole, 2 mM GTP, 1 mM BME, and pH 7.2
His elution	80 mM PIPES, 1 mM EGTA, 5 mM $MgCl_2$, 500 mM imidazole, 2 mM GTP, 1 mM BME, and pH 7.2
Strep binding	80 mM PIPES, 1 mM EGTA, 5 mM $MgCl_2$, 2 mM GTP, mM BME, and pH 7.2
Strep elution	80 mM PIPES, 1 mM EGTA, 4 mM $MgCl_2$, 2.5 mM D-desthiobiotin, 50 mM imidazole, 2 mM GTP, 1 mM BME, and pH 7.2
Storage	80 mM PIPES, 1 mM EGTA, 1 mM $MgCl_2$, 0.2 mM GTP, and pH 6.8

Materials and Methods

Purification of Recombinant Human Tubulin. Human tubulin was purified recombinantly as described previously (21). Briefly, cell pellets from 2 L of High Five insect cells expressing human TUBB3-TEVsite-StrepTagII, with the C-terminal StrepTagII cleavable by tobacco etch virus (TEV) protease, and TUBA1B-$His^{internal}$ (wt, E254A, or E254D) were resuspended 1:1 (vol/vol) in cold lysis buffer and lysed by douncing 60 times. Lysate was diluted fourfold in dilution buffer and clarified by ultracentrifugation (158,420 × g, 1 h, 4 °C). The supernatant was passed through a 5-mL HisTrap HP column (GE Healthcare), and the eluate was immediately diluted six times in Strep buffer and passed through a 1-mL HiPrep SP FF column, followed by a 5-mL StrepTrap HP column (GE Healthcare). Tubulin was eluted off the column, diluted twofold in Strep elution buffer, and incubated on ice for 2 h with TEV protease to remove the StrepTagII from TUBB3. The eluate was then clarified by ultracentrifugation (204,428 × g, 10 min, 4 °C). The supernatant was passed through a 1-mL HiPrep SP FF column, desalted into storage buffer, concentrated to 3.5 mg/mL, ultracentrifuged (278,088 × g, 10 min, and 4 °C), and flash frozen in 10 μL aliquots with liquid nitrogen (Table 2).

Purification of EB3. Monomeric EB3 used for cryo-EM was purified as previously described (8, 33). Human $EB3_{1–200}$ was inserted into a 2BT vector with a C-terminal His-tag (Macrolab, University of California, Berkeley [UC Berkeley]) and expressed in BL21(DE3)-RIL *Escherichia coli*. Cell pellets from a 2-L culture were resuspended in 1:2 (vol/vol) lysis buffer and lysed by sonication. Cell debris was pelleted by centrifugation (18,000 × g, 45 min, 4 °C), and supernatant was loaded on a 5-mL HisTrap column (GE Healthcare) and eluted with a 0 to 100% gradient of lysis buffer to elution buffer. The elution was incubated with TEV protease overnight at 4 °C to remove the His-tag, followed by a subtractive nickel purification to remove TEV, uncleaved EB3, and the His-tag. The flow-through was concentrated to 500 μL and loaded on a Superdex 200 10/300 GL pre-equilibrated in SEC buffer for size-exclusion chromatography. Peak fractions were pooled, concentrated to 20 μM, and flash frozen in SEC buffer until needed (Table 3). mGFP-EB3 used for TIRF microscopy was purified as described (21).

Purification of Kinesin. The kinesin plasmid was generously supplied by the Vale laboratory (35) and purified as described previously (5). The plasmid encoding His_6-tagged, monomeric, catalytically inactive Kif5b (1 to 350aa, E236A) was transformed into BL21(DE3) cells for expression. Upon reaching optical density $(OD)_{600}$ = 0.5, the 1-L expression culture was brought to 22 °C and induced with 0.2 mM IPTG (isopropyl ß-D-1-thiogalactopyranoside) for 16 h. The cells were harvested with by centrifugation at 4,000 g for 20 min at 4 °C. Cell pellets were resuspended in lysis buffer and incubated at room temperature for 30 min followed by sonication (3 × 45 s, at power level 7). The lysate was clarified by centrifugation at 30,000 g for 60 min, and the supernatant was then incubated with Nickel-NTA beads (GE Healthcare). The protein was washed with 6 column volumes of wash buffer and eluted with 2 column volumes of elution buffer. The elution was pooled and loaded onto a size-exclusion column equilibrated with SEC buffer. Fractions were analyzed by SDS-PAGE (sodium dodecyl sulphate–polyacrylamide gel electrophoresis) for kinesin, and peak fractions were pooled and concentrated to 20 μM before flash-freezing in liquid nitrogen until needed (Table 4).

Table 3. Buffers for the purification of monomeric EB3

Lysis	50 mM Tris pH 8.0, 150 mM NaCl, 1 mM EDTA, 1 mM DTT + protease inhibitors, DNase, RNase, and Lysozyme
His elution	50 mM Tris pH 8.0, 150 mM NaCl, 1 mM EDTA, 1 mM DTT, and 300 mM imidazole
SEC buffer	50 mM Tris pH 8.0, 150 mM NaCl, 1 mM EDTA, 1 mM DTT, and 10% glycerol

Cryo-EM Sample Preparation. Cryo-EM specimens were prepared on CFlat 1.2/1.3-T open-hole grids (Protochips) that were plasma cleaned for 30 s with a Tergeo plasma cleaner (Pie Scientific). A 10-μL aliquot of tubulin was thawed on ice for 10 min and supplemented with 0.05% Nonidet P-40. The tubulin was incubated at 37 °C for 30 to 40 min to form MTs. While polymerizing, the Vitrobot Mark IV was equilibrated to the following conditions: 37 °C, 100% humidity, 15 blot force, and a 4-s blot with 1-s drain time. In total, 2 μL of MT solution was adsorbed onto the grid for 30 s followed by plunge freezing into a eutectic solution of liquid ethane/propane (70:30). For conditions in which Kinesin or EB3 were used to decorate the MT, two 4-μL aliquots of 20 μM kinesin/EB3 were added to the MT grid with a 30-s wait time in between additions to allow binding. Blotting conditions were identical for all mutants and decorating MT-associated proteins to maintain consistency.

Cryo-EM Data Collection. All grids were clipped and loaded into a Gatan Autoloader for imaging with a Titan Krios microscope at the Cal-Cryo EM facility in UC Berkeley. The data were collected with a Gatan Imagine Filter (GIF) energy filter and Gatan K2 or K3 camera (depending on the dataset) operating in superresolution mode. Data collection was controlled by SerialEM (36). Each micrograph had a total electron exposure of $40e^-$ collected over 40 frames and was collected within a defocus range of 0.8 to 2 μm. Collection parameters for each dataset are reported in *SI Appendix*, Table S1. The E254A structure was obtained over two different data collection sessions, because a more-thorough classification was necessary. It should be noted that the same grid was used for both sessions, and there was no bias in the number of the 13-pf 4-start particles (MT segments used in the image processing) for either of the data collections.

Cryo-EM Analysis and Model Building. Data processing was done mostly within the RELION framework (37). Final processing steps that are specific to MTs were performed in FREALIGN, which was necessary for identifying the correct seam location for undecorated MTs (38). Briefly, MotionCorr 2.1 5 × 5 patch-based alignment was performed on each micrograph (39). CTFFind4 was used to estimate the defocus of each micrograph (40). MTs were manually picked within RELION, and short, MT segments ("particles") were extracted with a repeat length of 82 Å. Initial pf classification was performed with RELION's Class3D function on bin4 data. Once the helical parameters were classified, particles within the same class (primarily 13 pf) were unbinned, recentered, and re-extracted. Unbinned particles were refined within RELION, and then converted into FREALIGN format for pseudohelical Fourier symmetrization to improve resolution, as well as to carry out SeamSearch protocols (29) to correctly identify the seam location. Data processing procedures are summarized in *SI Appendix*, Fig. S2.

Atomic models were built using a previous porcine MT structure as a template (Protein Data Bank: 6dpu), changing the necessary residues to account for the differences between porcine and human tubulins as well as the active site mutations. Each tubulin subunit was rigid-body docked with PHENIX and refined using the real-space refinement program within PHENIX (41, 42). All

Table 4. Buffers for the purification of kinesin

Lysis	50 mM $NaPO_4$ pH 8.0, 300 mM KCl, 2 mM $MgCl_2$, 10% glycerol, 10 mM Imidazole, and 1 mM DTT
Wash	50 mM $NaPO_4$ pH 8.0, 150 mM KCl, 2 mM $MgCl_2$, 10% glycerol, 30 mM Imidazole, 1 mM DTT, and 200 μM ATP
Elution	50 mM $NaPO_4$ pH 8.0, 150 mM KCl, 2 mM $MgCl_2$, 10% glycerol, 250 mM Imidazole, and 1 mM DTT
SEC buffer	25 mM Tris pH 7.5, 150 mM KCl, 10% glycerol, 2 mM $MgCl_2$, and 2 mM DTT

refinements were treated with the same number of iterations to minimize variations in the processing procedure.

For the seam analysis (Fig. 5), atomic coordinates were rigid-body docked into both the C1 and pseudo-helical symmetry refined maps. The displacement was calculated using the *colorbyrmsd.py* script within PyMol (PyMOL Molecular Graphics System, Schrödinger LLC) and then normalized so that all samples were on the same scale from 0 to 1 Å. *Colorbyrmsd.py* was also used to calculate displacements between various MT states in *SI Appendix*, Fig. S3.

Determination of the MT Nucleotide Content. The nucleotide content of E254N MTs (*SI Appendix*, Fig. S1*B*) was determined by HPLC as described (21).

TIRF Microscopy Assay with Recombinant Human Tubulin Mutants. Dynamic MT assays with E254N tubulin were performed as described previously (21, 43). In brief, flow chambers were prepared from poly-(L-lysine)-polyethylene glycol (PEG) passivated microscopy slides and biotin-PEG–functionalized coverslips (44). Chambers were further passivated for 5 min at room temperature with 5% Pluronic F-127 (P2443, Sigma-Aldrich) and extensively washed with assay buffer (80 mM PIPES, 1 mM EGTA, 1 mM $MgCl_2$, 30 mM KCl, 1 mM GTP, 5 mM 2-ME, 0.15% [wt/vol] methylcellulose [4000 cP, Sigma-Aldrich], and 1% [w/vol] glucose, pH 6.8), followed by two washes with κ-casein (50 μg/mL in assay buffer, C0406, Sigma-Aldrich) in assay buffer. Neutravidin diluted in the κ-casein solution (50 μg/mL, A2666, Thermo Fisher Scientific) was flowed in, incubated for 3 min at room temperature, and washed out with assay buffer, followed by biotinylated GMPCPP porcine brain MT seeds labeled with CF640R (12% labeling ratio) diluted in assay buffer. After a final wash with assay buffer, the final reaction mix was flowed into the flow chamber. This mix included 98% unlabeled recombinant human E254N tubulin diluted in assay buffer containing oxygen scavengers (180 mg/mL catalase [C40, Merck] and 752 mg/mL glucose oxidase [22778.01, Serva]) and 2% mGFP-EB3 diluted in its storage buffer (50 mM Na-phosphate, 400 mM KCl, 5 mM $MgCl_2$, and 0.5 mM 2-ME, pH 7.2) to final concentrations of 12.5 mM E254N tubulin and 5 to 40 nM mGFP-EB3. Directly after sealing, the flow chamber was placed inside the microscope incubator at 30 °C and imaged after 2 to 3 min.

Data with E254A MTs were recorded previously (21). In brief, E254A MTs were polymerized from (nonimmobilized) fluorescent, biotinylated, GMPCPP-stabilized porcine brain MT seeds (0.5 μM polymerized tubulin) at 1 μM E254A tubulin for 1 h at 37 °C in BRB80 (80 mM PIPES, 1 mM EGTA, and 1 mM $MgCl_2$, pH 6.8) with 1 mM GTP. These stable MTs were stored at room temperature until use. Flow chambers were prepared as above, except that κ-casein was added to the chamber placed on a metal block on ice. Prepolymerized, stable MTs diluted in BRB80 were flowed into the chamber and attached to the neutravidin surface at room temperature. The chambers were then washed and imaged using 98% assay buffer with oxygen scavengers as above and supplemented with 2% mGFP-EB3 diluted in its storage buffer, yielding a final mGFP-EB3 concentration between 5 and 50 nM.

TIRF Microscopy Imaging. Dynamic TIRF microscopy assays with E254N tubulin and mGFP-EB3 were performed using a TIRF microscope (Cairn Research, Faversham, United Kingom) (43) with a 100× oil-immersion objective (Nikon CFI SR Apo, NA = 1.49) for 20 min at 1 frame/5 s with 300-ms exposure times for both MT seeds (using 640-nm laser excitation) and mGFP-EB3 (using 488-nm laser excitation). Several images in different fields of view were acquired 25 min after the initial temperature shift for the measurements of mGFP intensity profiles along the MTs. The data for stable E254A MTs with mGFP-EB3 are from a previous study (21) and were reanalyzed in detail here.

TIRF Microscopy Data Analysis. All images were processed using FIJI (version 1.53c, Research Resource Identifier [RRID]: SCR_002285) (45). Images were first corrected for uneven illumination using the FIJI rolling ball background subtraction algorithm with a radius of 50 pixels. As necessary, channels were aligned using a custom MATLAB script and reference images from a calibration slide (Argo-HM, Argolight, France). Then, segmented lines (3 pixels wide) were drawn along the longer MT segment elongating from the seed, excluding overlapping MTs. Line intensity profiles were averaged over their width. For each intensity profile, the local background was obtained by shifting the segmented line to the closest region without MTs and subtracted pixel-by-pixel. Background-subtracted intensity profiles were pooled together to generate mGFP-EB3 global intensity distributions and calculate their moments using OriginPro2021 (OriginLab, RRID: SCR_014212).

Kymographs from individual E245N MTs were obtained using custom FIJI macros to trace maximum-intensity projections. Periods of constant growth speed were inferred manually for each kymograph and their duration used as weight to calculate the mean E245N MT growth speed for the different mGFP-EB3 concentrations studied. Standard errors on the weighted mean were calculated following standard uncertainty propagation. The different mGFP-EB3 binding patterns to E245N MTs were categorized and quantified manually.

Data Availability. The following Cryo-EM maps and refined atomic coordinates have been deposited in the Electron Microscopy Data Bank: wt E254-GDP (EMD-25156, PDB-7SJ7); wt E254-GDP-Kinesin (EMD-25157, PDB-7SJ8); GTP-E254A 3-start (EMD-25158); GTP-E254A-EB3 (EMD-25159, PDB-7SJ9); GTP-E254N (EMD-25160, PDB-7SJA); and GTP-E254N-EB3 (EMD-25161).

ACKNOWLEDGMENTS. We thank Claire Thomas for help with expressing and purifying recombinant tubulin in insect cells, Abhiram Chintangal and Paul Tobias for support with computation, and Dan Toso, Jonathan Remis, and Patricia Grob for support with EM, as well as Simone Kunzelmann and Iain Taylor who helped with the determination of nucleotide content of E254N MTs by HPLC. We thank Juan Estévez-Gallego for critically reading the manuscript. B.J.L. was supported by NSF-Graduate Research Fellowship Program Grant 1106400. J.R., G.H., and T.S. were supported by the Francis Crick Institute, which receives its core funding from Cancer Research UK (FC001163), the UK Medical Research Council (FC001163), and the Wellcome Trust (FC001163). J.R. was supported by a Sir Henry Wellcome Postdoctoral Fellowship (100145/Z/12/Z). E.N. acknowledges support from the NIH (R35GM127018). T.S. acknowledges support from the European Research Council (Advanced Grant, project no. 323042). G.H., D.N., and T.S. acknowledge the support of the Spanish Ministry of Economy, Industry and Competitiveness to the CRG-EMBL partnership, the Centro de Excelencia Severo Ochoa, and the CERCA Programme of the Generalitat de Catalunya. T.S. also acknowledges support from the Miller Institute for Basic Research in Science at UC Berkeley. E.N. is a Howard Hughes Medical Institute Investigator.

1. G. J. Brouhard, L. M. Rice, Microtubule dynamics: An interplay of biochemistry and mechanics. *Nat. Rev. Mol. Cell Biol.* **19**, 451–463 (2018).
2. D. N. Drechsel, M. W. Kirschner, The minimum GTP cap required to stabilize microtubules. *Curr. Biol.* **4**, 1053–1061 (1994).
3. J. Howard, A. A. Hyman, Growth, fluctuation and switching at microtubule plus ends. *Nat. Rev. Mol. Cell Biol.* **10**, 569–574 (2009).
4. T. Mitchison, M. Kirschner, Dynamic instability of microtubule growth. *Nature* **312**, 237–242 (1984).
5. G. M. Alushin *et al.*, High-resolution microtubule structures reveal the structural transitions in αβ-tubulin upon GTP hydrolysis. *Cell* **157**, 1117–1129 (2014).
6. S. W. Manka, C. A. Moores, Microtubule structure by cryo-EM: Snapshots of dynamic instability. *Essays Biochem.* **62**, 737–751 (2018).
7. J. Richard McIntosh, E. O'Toole, C. Page, G. Morgan, Ultrastructural analysis of microtubule ends. *Methods Mol. Biol.* **2101**, 191–209 (2020).
8. R. Zhang, G. M. Alushin, A. Brown, E. Nogales, Mechanistic origin of microtubule dynamic instability and its modulation by eb proteins. *Cell* **162**, 849–859 (2015).
9. R. Zhang, B. LaFrance, E. Nogales, Separating the effects of nucleotide and EB binding on microtubule structure. *Proc. Natl. Acad. Sci. U.S.A.* **115**, E6191–E6200 (2018).
10. S. W. Manka, C. A. Moores, The role of tubulin-tubulin lattice contacts in the mechanism of microtubule dynamic instability. *Nat. Struct. Mol. Biol.* **25**, 607–615 (2018).
11. J. Estévez-Gallego *et al.*, Structural model for differential cap maturation at growing microtubule ends. *eLife* **9**, e50155 (2020).
12. M. Katsuki, D. R. Drummond, R. A. Cross, Ectopic A-lattice seams destabilize microtubules. *Nat. Commun.* **5**, 1–13 (2014).
13. E. M. Mandelkow, R. Schultheiss, R. Rapp, M. Müller, E. Mandelkow, On the surface lattice of microtubules: Helix starts, protofilament number, seam, and handedness. *J. Cell Biol.* **102**, 1067–1073 (1986).
14. D. Tong, G. A. Voth, Microtubule simulations provide insight into the molecular mechanism underlying dynamic instability. *Biophys. J.* **118**, 2938–2951 (2020).
15. P. Bieling *et al.*, CLIP-170 tracks growing microtubule ends by dynamically recognizing composite EB1/tubulin-binding sites. *J. Cell Biol.* **183**, 1223–1233 (2008).
16. P. Bieling *et al.*, Reconstitution of a microtubule plus-end tracking system in vitro. *Nature* **450**, 1100–1105 (2007).
17. R. Dixit *et al.*, Microtubule plus-end tracking by CLIP-170 requires EB1. *Proc. Natl. Acad. Sci. U.S.A.* **106**, 492–497 (2009).
18. C. Duellberg, N. I. Cade, D. Holmes, T. Surrey, The size of the EB cap determines instantaneous microtubule stability. *eLife* **5**, e13470 (2016).
19. Y. Komarova *et al.*, Mammalian end binding proteins control persistent microtubule growth. *J. Cell Biol.* **184**, 691–706 (2009).
20. S. P. Maurer, F. J. Fourniol, G. Bohner, C. A. Moores, T. Surrey, Ebs recognize a nucleotide-dependent structural cap at growing microtubule ends. *Cell* **149**, 371–382 (2012).
21. J. Roostalu *et al.*, The speed of GTP hydrolysis determines GTP cap size and controls microtubule stability. *eLife* **9**, e51992 (2020).
22. D. Roth, B. P. Fitton, N. P. Chmel, N. Wasiluk, A. Straube, Spatial positioning of EB family proteins at microtubule tips involves distinct nucleotide-dependent binding properties. *J. Cell Sci.* **132**, jcs219550 (2018).
23. D. Seetapun, B. T. Castle, A. J. McIntyre, P. T. Tran, D. J. Odde, Estimating the microtubule GTP cap size in vivo. *Curr. Biol.* **22**, 1681–1687 (2012).

24. L. Amos, A. Klug, Arrangement of subunits in flagellar microtubules. *J. Cell Sci.* **14**, 523–549 (1974).
25. S. Chaaban, G. J. Brouhard, A microtubule bestiary: Structural diversity in tubulin polymers. *Mol. Biol. Cell* **28**, 2924–2931 (2017).
26. L. G. Tilney *et al.*, Microtubules: Evidence for 13 protofilaments. *J. Cell Biol.* **59**, 267–275 (1973).
27. A. Vemu *et al.*, Structure and dynamics of single-isoform recombinant neuronal human tubulin. *J. Biol. Chem.* **291**, 12907–12915 (2016).
28. A. D. Cook, S. W. Manka, S. Wang, C. A. Moores, J. Atherton, A microtubule RELION-based pipeline for cryo-EM image processing. *J. Struct. Biol.* **209**, 107402 (2020).
29. R. Zhang, E. Nogales, A new protocol to accurately determine microtubule lattice seam location. *J. Struct. Biol.* **192**, 245–254 (2015).
30. D. Chrétien, S. D. Fuller, Microtubules switch occasionally into unfavorable configurations during elongation. *J. Mol. Biol.* **298**, 663–676 (2000).
31. A. Vemu, J. Atherton, J. O. Spector, C. A. Moores, A. Roll-Mecak, Tubulin isoform composition tunes microtubule dynamics. *Mol. Biol. Cell* **28**, 3564–3572 (2017).
32. A. A. Hyman, D. Chrétien, I. Arnal, R. H. Wade, Structural changes accompanying GTP hydrolysis in microtubules: Information from a slowly ydrolysable analogue guanylyl-(alpha,beta)-methylene-diphosphonate. *J. Cell Biol.* **128**, 117–125 (1995).
33. S. P. Maurer, P. Bieling, J. Cope, A. Hoenger, T. Surrey, GTPgammaS microtubules mimic the growing microtubule end structure recognized by end-binding proteins (Ebs). *Proc. Natl. Acad. Sci. U.S.A.* **108**, 3988–3993 (2011).
34. E. H. Kellogg *et al.*, Insights into the distinct mechanisms of action of taxane and non-taxane microtubule stabilizers from cryo-EM structures. *J. Mol. Biol.* **429**, 633–646 (2017).
35. S. Rice *et al.*, A structural change in the kinesin motor protein that drives motility. *Nature* **402**, 778–784 (1999).
36. M. Schorb, I. Haberbosch, W. J. H. Hagen, Y. Schwab, D. N. Mastronarde, Software tools for automated transmission electron microscopy. *Nat. Methods* **16**, 471–477 (2019).
37. J. Zivanov *et al.*, New tools for automated high-resolution cryo-EM structure determination in RELION-3. *eLife* **7**, e42166 (2018).
38. N. Grigorieff, FREALIGN: High-resolution refinement of single particle structures. *J. Struct. Biol.* **157**, 117–125 (2007).
39. S. Q. Zheng *et al.*, MotionCor2: Anisotropic correction of beam-induced motion for improved cryo-electron microscopy. *Nat. Methods* **14**, 331–332 (2017).
40. A. Rohou, N. Grigorieff, CTFFIND4: Fast and accurate defocus estimation from electron micrographs. *J. Struct. Biol.* **192**, 216–221 (2015).
41. P. D. Adams *et al.*, PHENIX: A comprehensive Python-based system for macromolecular structure solution. *Acta Crystallogr. D Biol. Crystallogr.* **66**, 213–221 (2010).
42. P. V. Afonine *et al.*, New tools for the analysis and validation of cryo-EM maps and atomic models. *Acta Crystallogr. D Struct. Biol.* **74**, 814–840 (2018).
43. J. Hannabuss *et al.*, Self-organization of minimal anaphase spindle midzone bundles. *Curr. Biol.* **29**, 2120–2130 (2019).
44. P. Bieling, I. A. Telley, C. Hentrich, J. Piehler, T. Surrey, Fluorescence microscopy assays on chemically functionalized surfaces for quantitative imaging of microtubule, motor, and +TIP dynamics. *Methods Cell Biol.* **95**, 555–580 (2010).
45. J. Schindelin *et al.*, Fiji: An open-source platform for biological-image analysis. *Nat. Methods* **9**, 676–682 (2012).